Ultrathin Chalcogenide Nanosheets for Photoacoustic Imaging-Guided Synergistic Photothermal/Gas Therapy

Jingjing Wu,[†] Gareth R. Williams,[‡] Yu Zhu,[†] Tingting Hu,[†] Hui Wang,[†] Wei Zhao,[†] Ruizheng Liang,*[†] Xisheng Weng,*[§] Min Wei*[†]

[†]*State Key Laboratory of Chemical Resource Engineering, Beijing Advanced Innovation Center for Soft Matter Science and Engineering, Beijing University of Chemical Technology, Beijing 100029, P. R. China*

[‡]*UCL School of Pharmacy, University College London, 29-39 Brunswick Square, London WC1N 1AX, UK*

[§]*Department of Orthopaedics, Peking Union Medical College Hospital, Peking Union Medical College & Chinese Academy of Medical Sciences, Beijing 100730, China*

E-mail addresses: liangrz@mail.buct.edu.cn (R. Liang); xshweng@medmail.com.cn (X. Weng); weimin@mail.buct.edu.cn (M. Wei).

Abstract

Previous preclinical and clinical studies have shown that using only a single therapy makes it difficult to completely eradicate tumors and restrain cancer metastasis. To overcome this challenge, multi-modal synergistic treatments have attracted considerable attention. Herein, an ultrathin Cu-loaded CoCuFe-selenide (CCFS) was prepared by a facile topotactic transformation from CoCuFe layered double hydroxide (LDH) nanosheets (NSs), followed by surface modification with polyvinyl pyrrolidone (PVP) and L-arginine (L-Arg). The resultant CCFS-PVP-L-Arg (CPA) system shows excellent synergetic photothermal and gas therapy (PTT/GT). The CCFS NSs have strong LSPR absorbance characteristic, with enhanced light absorption in the near-infrared (NIR) region. This endows the CPA nanocomposite with an outstanding photothermal conversion efficiency of 72.0% (pH 7.4) and 81.0% (pH 5.4), among the highest reported for 2D chalcogenide nanomaterials. In addition, NO release from CPA is triggered by decomposition of L-Arg in the H_2O_2-rich and acidic tumor microenvironment, permitting localized NO gas therapy in the tumor site. *In vitro* experiments revealed 91.8% apoptosis of HepG2 cells, and *in vivo* studies showed complete tumor elimination upon treatment with the CPA nanocomposite under NIR irradiation. To the best of our knowledge, this is the first report of combined defect-induced high-efficiency PTT with H_2O_2 and pH targeted GT.

1. Introduction

Photothermal therapy (PTT), an emerging cancer treatment strategy, has attracted tremendous attention in recent years since it is minimally invasive with high regional selectivity and low toxicity [1-4]. PTT commonly utilizes photothermal agents to generate localized hyperthermia under near-infrared (NIR) light irradiation, leading to thermally-driven tumor ablation. Therefore, the design and synthesis of PTT agents with high NIR to heat conversion efficiency is key to attaining satisfactory PTT performance [5]. Recently, many photothermal agents have been exploited for the PTT of cancer, including black phosphorus, 2D boron NSs, antimonene-based nanomaterials, ultrathin chalcogenide NSs and organic dyes (*i.e.*, indocyanine green), among which 2D transition metal chalcogenide nanosheets (TMC NSs) have received significant attention because of their tunable band gaps and versatile properties [6-11]. The quantum confinement effect enables TMC NSs to possess favorable optical properties and electronic band structure, resulting in thickness-dependent NIR absorption characteristics and efficient photothermal conversion properties. Materials such as MoS_2, $MoSe_2$, and WSe_2 have been found to be promising candidates for PTT [12-16]. Moreover, the presence of multiple (>2) metal ions in TMC NSs has been shown to give enhanced photothermal conversion efficiency (PCE) for PTT over mono- and dual-metal TMC NSs [17]. In spite of the great progress in this field, the inhomogeneous heat distribution within tumor tissues of NIR therapy alone makes it difficult for PTT to completely eradicate tumors and restrain metastasis [18-24], however. Routes to combine PTT with other treatment modalities to achieve significantly enhanced therapeutic outcomes remain much sought after.

Gas therapy (GT) is a "green" anticancer therapeutic strategy involving the use of gasotransmitters to induce cancer cell death [25]. A range of gaseous molecules, including hydrogen (H_2), hydrogen sulfide (H_2S), sulfur dioxide (SO_2), and nitric oxide (NO), can be used in GT

[26-31]. Among these, NO is a particularly attractive candidate for exploitation, since it can participate in a variety of physiological and pathological activities [32]. For instance, NO directly causes cell death at a relatively high concentration, and shows excellent synergistic effects when combined with other therapeutic methods [33]. L-arginine (L-Arg) can be used as a NO precursor, releasing NO only in H_2O_2-rich and acidic tumor microenvironments [34]. This can result in targeted GT and efficiently avoid unwanted NO release in healthy tissues. Cu-based chalcogenides such as CuS, $Cu_{2-x}Se$ and CuTe, have been reported to be efficient photothermal agents owing to their localized surface plasmon resonance (LSPR) characteristics [35-39]. This inspired us to consider whether we can increase the presence of defect vacancies in these chalcogenides by adjusting the Cu doping ratio or using surface corrosion to produce more free charge carriers. This should resonate with incident radiation and promote LSPR absorption, thereby enhancing the photothermal performance. Moreover, if Cu-based chalcogenides were further modified with L-Arg, targeted NO release and synergistic PTT and GT would be realized.

Currently, a variety of methods including mechanical-exfoliation (ME), intercalation-assisted exfoliation, sonication-assisted liquid exfoliation, chemical vapor deposition (CVD) and wet-chemical synthesis have been developed to prepare ultrathin TMC NSs [40-44]. However, there are still some significant challenges in facile operation, uniform morphology, ingenious regulation and mass production. Moreover, TMC NSs prepared by the above methods generally have issues of unsatisfactory photothermal conversion efficiency (η) and PTT behavior. Therefore, an ingenious route to synthesize TMC NSs with superior therapeutic and diagnostic performance will be essential for future clinical cancer therapy. Layered double hydroxide nanosheets (LDH NSs) are a class of two-dimensional (2D) nanomaterials with positive layers containing metal ions and charge balancing interlayer anions. The metal composition is highly tuneable, and thus LDH NSs have

been widely explored in catalysis, energy storage, electrochemistry and biomedicine [45-54]. In this work, Cu-based CoCuFe-selenide (CCFS) NSs were prepared *via* an *in situ* selenylation treatment of an ultrathin CoCuFe-LDH precursor. Subsequently, further surface modification was undertaken with polyvinyl pyrrolidone (PVP) and L-Arg, generating a CCFS-PVP-L-Arg (CPA) nanocomposite which was explored in detail for its potential in synergistic PTT/GT. The CPA nanocomposite is found to have the Co_9Se_8 structure, with a uniform size of ~85 nm and a thickness of ~2.0 nm. The PTT efficiency of CPA could be controlled by regulating the Cu doping ratio, with an optimal PCE of 72.0% at a 30% Cu molar content at pH 7.4. This further increased to 81.0% at pH=5.4 (simulating the acidic tumor microenvironment). Simultaneously, the CPA nanocomposite displays a superior PA imaging capability with an ultralow detection limit (5 ppm) by virtue of the excellent photothermal performance. Moreover, a burst release of NO was achieved under acidic and H_2O_2 enriched conditions, indicating targeted and tumor-specific gas therapy. *In vitro* and *in vivo* tests show 91.8% apoptosis of HepG2 cells and complete tumor elimination after treatment with the CPA nanocomposite under NIR irradiation. Therefore, it is clear that ultrathin Cu-based chalcogenide NSs combined with tumor-specific NO donors can serve as efficient and targeted systems for future clinical cancer theranostics.

2. Experimental Section

2.1 Synthesis of CoCuFe-LDH nanosheets (NSs) precursor

CoCuFe-LDH NSs with various Cu contents were prepared by a bottom-up method previously reported by our group, with some modifications. Solution A was prepared by combining $Co(NO_3)_2 \cdot 6H_2O$ (a mol, a = 0.00216, 0.00192, 0.00168, 0.00144 mol), $Cu(NO_3)_2 \cdot 3H_2O$ (b mol, a + b = 0.0024 mol) and $Fe(NO_3)_3 \cdot 9H_2O$ (0.0006 mol) in 60 mL of deionized water. Solution B

comprised 54 mL of an aqueous NaOH solution (0.0135 mol); Solution C contained $NaNO_3$ (0.0006 mol) and 13.8 mL formamide dissolved in 46.2 mL of deionized water. Solution A and B were added dropwise into solution C with stirring at 80 °C. The resultant colloidal precipitate was washed with water and ethanol several times and centrifuged at a speed of 7000 rpm for 5 min. Dialysis was then performed against deionized water with a 3 kDa dialysis membrane used to remove excess formamide. The resulting CoCuFe-LDH colloid was redispersed in ethanol.

2.2 Synthesis of CCFS NSs

CCFS NSs were obtained *via* a facile *in situ* selenylation reaction of CoCuFe-LDH. Briefly, 0.0005 mol of the as-prepared CoCuFe-LDH NSs were dispersed in 60 mL of ethanol. A NaHSe solution was prepared by introducing $NaBH_4$ (0.0015 mol) into Se powder (0.0005 mol) with gentle stirring for 10 min. The NaHSe solution was then mixed with the CoCuFe-LDH suspension under flowing N_2 protection. After magnetic stirring for 10 min at room temperature, the black suspension obtained was transferred into a 100 mL autoclave and crystallized at 180 °C for 2, 4, 6, 8, 12, 16 h, respectively. After cooling to room temperature in air, the resulting CCFS NSs were purified with water and ethanol several times and centrifuged at 7000 rpm for 5 min. The CCFS NSs were re-dispersed in deionized water for further modification.

2.3 Synthesis of CPA nanocomposite

PVP (50 mg) and L-Arg (50 mg) were added into 10 mL of the aqueous CCFS NS suspension (500 μg mL^{-1}). After 12 h of stirring at room temperature, the mixture was centrifuged at 7000 rpm for 5 min. The CPA nanocomposite was obtained after the precipitation was washed with deionized water three times to remove residual L-Arg or PVP in solution.

2.4 NO gas generation

The NO production ability of CPA was evaluated using a micro NO content assay kit (Solarbio

Science &Technology Co., Ltd., Beijing, China). Three sets of conditions were explored: (1) CPA/free H_2O_2; (2) CPA+ H_2O_2 (10 mM) at pH 7.4; (3) CPA+ H_2O_2 (10 mM) at pH 6.5. The reaction suspensions were added to a 96-well plate, and after treatment with the reagents in the kit according to the manufacturer's instructions the absorption at 550 nm was measured with a microplate reader.

2.5 Cell culture

U87mg, Hela, HepG2 and COS7 cells were separately cultured in Dulbecco's modified eagle's medium (DMEM) containing 1% v/v penicillin-streptomycin solution and 10% v/v fetal bovine serum (FBS), in an incubator (Thermo Scientific) with an atmosphere of 5% CO_2 at 37 °C. 1.0 mL of trypsin (0.25%) was used to digest cells and subculture.

2.6 Cytotoxicity assay

Cytotoxicity studies of CPA were carried out using the MTT method. Briefly, U87mg, Hela, HepG2 or COS7 cells (1×10^4 cells/well, 200 μL) were seeded in 96-well plates and incubated for 24 h. After adding the CPA nanocomposite at various concentrations (2, 5, 10, 20, 30, 50, 100 and 200 μg mL^{-1}), the cells were incubated for another 24 h. Subsequently, cell viability was determined by the colorimetric MTT method after washing with PBS 3 times. In addition, cells were seeded in 12-well plates and incubated with different concentrations (2, 5, 10, 20, 30, 50, 100 and 200 μg mL^{-1}) of CPA (1×10^5 cells/well, in 200 μL of medium). After incubation for 24 h, the culture medium was removed and the cells washed with PBS 3 times. Subsequently, cells were treated with Calcein-AM (5 μg mL^{-1}) and PI (10 μg mL^{-1}) for 20 min, allowing visualization of the population of lived and dead cells under a fluorescence microscope (Leica TCS SP5, Germany).

2.7 *In vitro* anticancer properties

HepG2 cells were seeded into 96-well plates (1×10^4 cells/well, 200 μL) for a 24 h incubation,

and then treated with LDH, CPA and CPA+H_2O_2 at different concentrations (2, 5, 10 and 20 μg mL^{-1}) for another 24 h. The culture medium was removed, the cells washed with PBS three times, and fresh medium added. Next, the LDH or CPA-treated cells were irradiated with an 808 nm laser at a power intensity of 1.0 W cm^{-2} for 10 min. The cells incubated with CPA+H_2O_2 were either exposed to the 808 nm laser (1.0 W cm^{-2}) for 10 min or left without any further treatment. Subsequently, cell viability was analyzed using the MTT assay, with calcein-AM/PI assays used to validate the MTT results. The pattern of cell apoptosis and necrosis was explored after staining using an Annexin V-FITC and PI staining kit and assay by flow cytometry (CytoFLEX, Beckman Coulter).

2.8 NO content in cells

NO generation in cells exposed to CPA was investigated using DAF-FM DA. HepG2 cells were seeded in 12-well plates and incubated in a 5% CO_2 atmosphere at 37 °C for 24 h. CPA was added into the cells and the plate incubated for another 24 h. After changing the medium at pH 6.5, HepG2 cells were given three different treatments: (1) CPA, (2) CPA+ H_2O_2 (0.1 mM), and (3) CPA+ H_2O_2 (0.1 mM) with 808 nm (1.0 W cm^{-2}) NIR irradiation for 10 min. The cells were then incubated for a further 4 h, and DAF-FM DA was added. The cells were incubated in the dark for 20 h and then imaged using a fluorescence microscope. Similarly, the fluorescence signal intensity was quantified by flow cytometry after incubation for 20 h in the dark.

2.9 PA imaging experiments

In vitro and *in vivo* PA imaging was performed on a multispectral optical tomography system (MSOT inVision 128, iThera Medical, Germany). A series of CPA and LDH aqueous suspensions (5, 10, 15, 20 and 25 μg/mL) was prepared in agar gel cylinders for *in vitro* testing. To investigate the imaging performance *in vivo*, tumor-bearing mice were *i.v.* injected with the CPA nanocomposite

(10 mg kg^{-1}, 200 μL), and PA signals were recorded at 0, 2, 4, 8, 12 and 24 h post-injection.

2.10 *In vivo* anti-tumor therapy

PBS suspensions of the CPA nanocomposite (10 mg kg^{-1}, 200 μL), or controls comprising PBS alone or an LDH suspension at the same concentration were *i.v.* injected into tumor-bearing mice. 8 h post-injection, the tumor sites were irradiated with an 808 nm NIR laser (1.0 W cm^{-2}) for 7 min. Control animals were not irradiated. The real-time changes in temperature at the tumor sites were monitored with a thermal imaging camera (Fluke Ti480, USA) during treatment. The tumor size was measured with calipers every 2 days for 16 days after irradiation treatment. The relative tumor volume was calculated as V/V_0 (V and V_0 are the tumor volume measured at time t and t_0, respectively). The body weight was measured every two days also.

2.11 Histological analysis

Mice were sacrificed and their tumors and main organs resected after 16 days of treatment. All the tissues were dipped in 10% formalin, cut into slices with 3-5 μm thickness, and stained with hematoxylin and eosin (H&E). The histology and morphology of slices were captured with a digital microscope (Leica TCS SP5, Germany).

2.12 Blood analysis

Healthy male Balb/c mice were *i.v.* injected with PBS and CPA samples (200 μL, 10 mg kg^{-1}). Blood samples were collected from the mice after 1 day and 7 days. Subsequently, blood biochemistry, liver function and kidney function indicators were measured.

2.13 Biodistribution

Tumor-bearing mice were *i.v.* injected with 200 μL of a PBS suspension of the CPA nanocomposite (10 mg kg^{-1}) and sacrificed 2, 4, 6, 8, 10, 12, 24 and 48 h after injection to collect the main organs (*i.e.*, heart, liver, spleen, lung, and kidneys). These tissues were digested with nitric

acid and the concentration of Co determined by ICP-MS.

2.14 4T1-Fluc tumor orthotopic mouse model

The orthotopic tumor model was established by injecting 4T1 cells (5×10^6, 100 µL in PBS) into the right fourth breast fat-pad of Balb/c mice. Mice with a tumor volume of around 70 mm^3 were selected for subsequent experiments.

2.15 *In vivo* bioluminescence imaging

The 4T1 tumor-bearing mice were injected with PBS, a suspension of the CPA nanocomposite (200 µL, 10 mg kg^{-1}) or an LDH suspension (200 µL, 10 mg kg^{-1}), and irradiated with an 808 nm NIR laser (1.0 W cm^{-2}) for 7 min after 8 h post-injection. Control animals did not receive the NIR treatment. To monitor tumor growth, the D-luciferin probe (150 mg kg^{-1}) was intraperitoneally injected into the mice, and imaging was performed every other day with an IVIS Lumina fluorescence imaging system.

2.16 Statistical analysis

Data are expressed as mean ± standard deviation (s.d). Statistical comparisons were made using an unpaired Student's t-test (between two groups) or one-way ANOVA (for multiple comparisons) followed by Tukey's post-test: $*p < 0.05$, $**p < 0.01$, $***p < 0.001$.

3. Results and discussion

3.1 Synthesis and characterization

The CCFS NSs were synthesized by a facile two-step method as illustrated in Figure 1a. Firstly, CoCuFe-LDH NSs as precursors were prepared *via* a "bottom-up" synthesis method [55]. Secondly, CCFS NSs were successfully fabricated by *in situ* selenylation of the CoCuFe-LDH precursors. Transmission electron microscopy (TEM) and atomic force microscopy (AFM) images reveal that

monodispersed plate-like CoCuFe-LDH NSs were formed, with a uniform size of ~70 nm and a thickness of ~1.3 nm (Figure 1b-d). After the selenylation reaction, the resulting CCFS NSs retain the plate-like morphology of the LDH precursor with unaltered size and thickness (Figure 1e-g). A homogeneous distribution of Co, Cu, Fe and O elements in the CoCuFe-LDH (Figure 1h) and of Co, Cu, Fe and Se in the CCFS NSs (Figure 1i) are observed by energy-dispersive X-ray (EDX) mapping, further confirming successful selenylation.
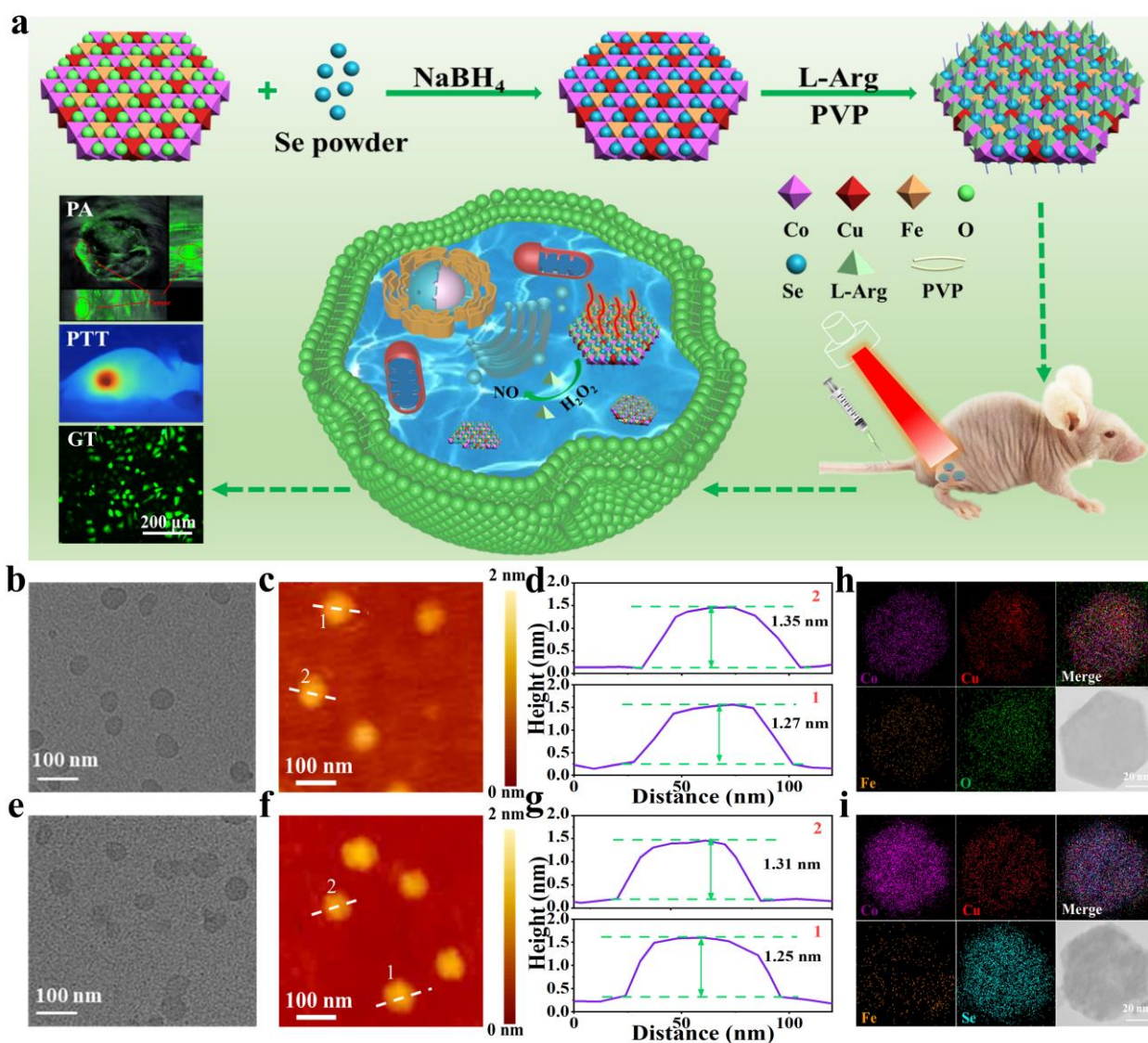

Figure 1. (a) A schematic illustration of the preparation of the CPA nanocomposite for PA image-guided synergistic PTT/GT. (b, e) TEM images, (c, f) AFM images, (d, g) corresponding thickness, and (h, i) EDX mapping of CoCuFe-LDH and CCFS NSs, respectively.

XRD was used to characterize the transformation of the crystal structure from CoCuFe-LDH to CCFS NSs. As shown in Figure S1, typical (003), (006) and (009) reflections were observed in CoCuFe-LDH, with the diffraction intensity decreasing gradually with the increase of copper content. For CCFS NSs, all the peaks could be well indexed with the Co_9Se_8 phase (JCPDS Card No. 09-0233) (Figure S2), indicating that the selenylation treatment of CoCuFe-LDH leads to the formation of Co_9Se_8 with Fe and Cu doping into the lattice. The structural transformation process with different reaction times was investigated (Figure S3). A selenylation time of 16 h was necessary for high crystallinity of CCFS NSs, and 16 h was thus used to generate all the CCFS samples for subsequent exploration.

The diffraction intensity of the resulting CCFS NSs gradually decreases as the Cu ratio increases from 10% to 40%, and some impurity phase appears at 40% Cu doping (Figure 2a). Inductively coupled plasma atomic emission spectrometry (ICP-AES) results show that the Cu ratio in the product is consistent with the feed ratio from 10% to 40% (Table S1). X-ray photoelectron spectroscopy (XPS) was used to explore the chemical composition and valence state of the CCFS NSs (Figure 2b). Peaks at 780.9 and 796.8 eV are assigned to Co^{2+} $2p_{3/2}$ and $2p_{1/2}$; those at 933.7 and 953.8 eV are attributed to Cu^{2+} $2p_{3/2}$ and $2p_{1/2}$; and, peaks at 931.9 and 951.7 eV belong to Cu^{+} $2p_{3/2}$ and $2p_{1/2}$; Peaks at 932.5 and 952.5 eV correspond to Fe^{3+} $2p_{3/2}$ and $2p_{1/2}$. A small amount of Co^0 $2p_{3/2}$ and $2p_{1/2}$ is observed at 778.3 and 793.2 eV, while the feature at 59.2 eV is relative to the surface oxidation of Se (SeO_x) (Figure 2c-f). All these observations confirm successful formation of the CCFS formulation.

The NO molecule has good diffusion ability in tumor tissues. It has also been reported as a secondary messenger that can regulate many physiological processes. L-Arg can react with H_2O_2 to generate NO under the acidic and H_2O_2-rich tumor microenvironment (TME) conditions. Therefore,

L-Arg was loaded onto the CCFS NSs for synergistic PTT/GT treatment. PVP was further used for surface modification to enhance the stability and biocompatibility. The resultant CPA nanocomposite shows a lateral size of ~85 nm and a thickness of ~2.0 nm (Figure S4 and S5). Fourier transform infrared spectroscopy (FT-IR) was further performed to verify successful functionalization with L-Arg and PVP (Figure 2g). M-Se vibrations at 711 cm^{-1} as well as L-Arg COO- symmetric stretching vibration at 1421 cm^{-1} and PVP C=O stretching vibration at 1660 cm^{-1} are observed with the CPA nanocomposite, which indicates L-Arg and PVP are successfully loaded. Thermogravimetric analysis (TGA) of CPA and CP was performed to assess the loading capacity, and the mass ratio of L-Arg in the final CPA was measured to be 5.6% by thermogravimetry (Figure S6). The physicochemical properties of the CCFS with 30% Cu content and CPA samples were further investigated. CCFS NSs with 30% Cu content show a negative zeta potential of -11.4 ± 0.1 mV in aqueous solution, while the LDH sample has a potential of 31.2 ± 0.1 mV. After the CCFS NSs are loaded with L-Arg and modified with PVP, the zeta potential changes to -34.1 ± 0.2 mV in water, with similar values obtained in Dulbecco's modified eagle's medium (DMEM) and phosphate-buffered saline (PBS) (Figure 2h). The hydrodynamic diameter of the CCFS NSs with 30% Cu content is measured to be 80 ± 3.7 nm (Figure S7a) by dynamic light scattering, which is close to that of the CoCuFe-LDH (84 ± 6.5 nm, Figure S7b). The CPA material in each of the three different media (water, PBS, and DMEM) displays an increased diameter of 113 ± 1.5 nm (Figure 2i). The excellent storage stability of CPA was demonstrated by the unaltered hydrodynamic size and Tyndall effect within a week storage period (Figure S8 and S9).
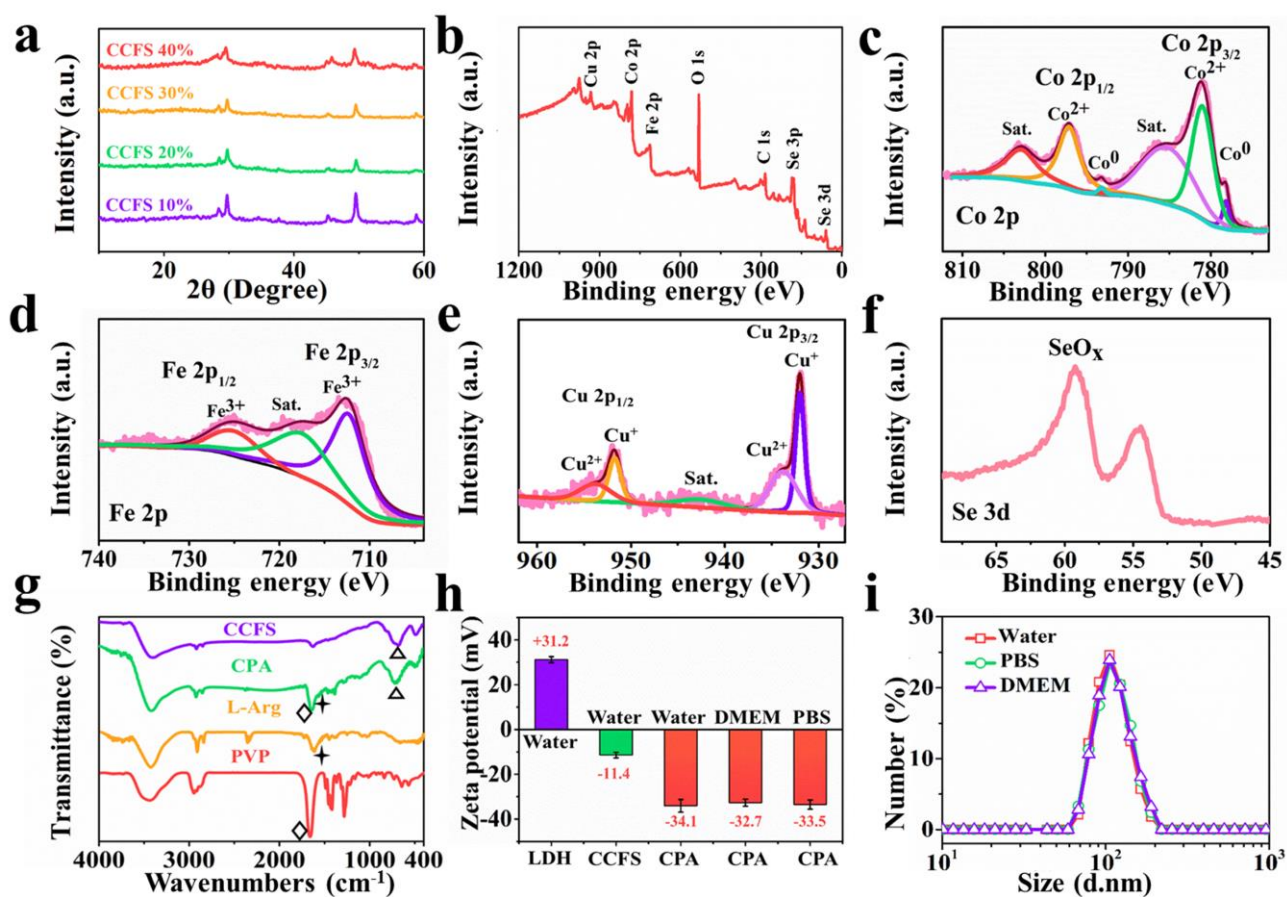
Figure 2. (a) XRD spectra of CCFS NSs with 10%, 20%, 30% and 40% Cu. (b) Survey XPS spectrum of CCFS NSs with 30% Cu content. (c) Co 2p, (d) Fe 2p, (e) Cu 2p, (f) Se 3d XPS spectra of the CCFS NSs with 30% Cu content. (g) FT-IR spectra of PVP, L-Arg, CCFS and CPA with 30% Cu content. (h) Zeta potential of LDH, CCFS with 30% Cu content and CPA samples in water, PBS and DMEM. (i) Size distribution of CPA in water, PBS and DMEM. Error bars denote ± s.d. (n = 3).

3.2 Photothermal properties and NO release of CPA nanocomposite

The influence of Cu-doped ratio on the PTT performance of the CPA nanocomposite was studied. NIR absorption of the CCFS NSs with various Cu ratios was recorded, and CCFS NSs with 30% Cu show a maximum absorbance at 808 nm. The CPA nanocomposite, prepared from 30% Cu-doped CCFS NSs, has almost the same absorbance at 808 nm (Figure 3a). The photothermal performance of the CCFS and CPA systems were evaluated by recording the temperature change

upon 808 nm (1.0 W cm^{-2}) laser irradiation. As shown in Figure 3b, the temperature change (ΔT) of CCFS with various Cu contents increases from 10% to 30% Cu and then decreases from 30% to 40%. The CCFS sample with 30% Cu thus possesses the best photothermal performance, consistent with the NIR absorption data. The ΔT of CPA decreases slightly compared to that of the 30% Cu CCFS NSs, but is nevertheless still very high.

The photothermal performance of CPA is strongly dependent on its concentration and laser power density (Fig. 3c and Figure S10): an increase in temperature (from 23.6 °C to 45.9 °C) is observed with the rise of concentration (10, 20, 30 and 50 ppm), and ΔT can be finely tuned from 12.9 °C to 45.9 °C by enhancing the laser power density (0.05, 0.3, 0.55, 0.75 and 1.0 W cm^{-2}). The temperature of changes could additionally be seen using an infrared (IR) thermal camera (Figure 3d). Considering the mildly acidic nature of TME, we further evaluated the photothermal properties of CPA at different pH values. Compared with pH 7.4, the CPA absorption at 808 nm increases by 14.2% at pH 5.4 (Figure 3e). The maximum temperatures depicted in Figure 3f are 45.9 °C, 47.3 °C and 50.1 °C at pH 7.4, 6.5 and 5.4, respectively. The photothermal conversion efficiency values (η) of CPA at pH 7.4, 6.5 and 5.4 are 72.0%, 76.5% and 81.0%, respectively (Figure 3g, Figure S9), which are dramatically superior to those of the most reported TMC photothermal agents, such as WS$_2$-PVP (36.9%), TaS$_2$-PEG (39.0%), and Cu$_2$Se (50.89%) (Table S2). This verifies an enhanced photothermal conversion performance under acidic conditions. Subsequently, the photostability of the CPA nanocomposite was investigated, and its photothermal effect found to remain stable after five consecutive heating/cooling cycles (Figure 3h). CPA shows no significant change of UV-vis-NIR absorption spectrum after storage at different concentrations over 7 days (Figure S12), confirming its excellent storage stability. Subsequently, the ion release of CPA was analyzed by ICP-MS. As shown in Figure S13, the ion (Co, Cu and Fe) release behavior was studied at pH 7.4,

6.5 and 5.4. After 24 h, a less than 8.89% of ion release (Co, Cu and Fe) is observed, indicating the low decomposition efficiency of CPA sample. Although CPA does not perform as well as Xenes, Silicon and black phosphorus in degradation, the low decomposition efficiency might enhance its retention effect in tumor sites [6, 56-57].

Given the potent photothermal property of CCFS with a 30% Cu-doped ratio at pH 5.4, we further studied the influence of different contents of Cu and different pH conditions on defects. Previous reports have demonstrated that Cu-based semiconductors with an LSPR peak in the NIR region could be applied as photothermal transducers. In addition, the free charge carriers caused by vacancies in Cu-based semiconductors can resonate with incident radiation, further enhancing LSPR absorption to yield improved photothermal performance. Therefore, the influence of different contents of Cu in the doped CCFS NSs on defect presence was studied. The HRTEM images of the (222) lattice plane in the CCFS NSs directly display lattice defects (Figure 3i). As the Cu content increases, more defect points/areas are observed on the surface of the NSs. It should be noted from the atomic-resolution spherical aberration corrected TEM image that more defect points (marked with red circles) can be directly observed as the Cu content increases (Figure S14). Raman spectra were collected to gain further insight into the changes in crystal structure and defects with an increasing Cu content (Figure 3j). CCFS NSs with 10% Cu reveal a typical spectrum of cobalt selenide with a sharp peak around 656.4 cm^{-1} and a weaker peak around 479.6 cm^{-1}. The sharp peak around 177.6 cm^{-1} is associated with the Se-Se stretching vibration. With an increase of Cu content from 10% to 30%, the Raman peaks show a gradual broadening and red shift due to the gradual distortion of the crystal structure, further implying that CCFS with 30% Cu content has more lattice defects than those with 10% and 20% Cu content [58,59]. To substantiate the defect-facilitated photothermal conversion of CCFS NSs, we dipped CCFS NSs in buffers with various pH values

(pH 5.4, 6.5, 7.4) to produce different defect contents. High-resolution XPS spectra of Cu $2p_{3/2}$ (Figure S15) was applied to evaluate the ratio of Cu^+ and Cu^{2+} in CCFS NSs at pH 5.4, 6.5, 7.4. Semi-quantitatively, 70.86% Cu (I) in CCFS NSs was found at pH 5.4, 68.05% at pH 6.5 and 56.77% at pH 7.4 (Table S3). The higher Cu^+ content in CCFS NSs induced by the combination of Cu^{2+} and electrons reflected increased defects. Thus, CCFS NSs possess more defects at pH 5.4 than at pH 7.4 and 6.5, which is consistent with the photothermal conversion values at various pH conditions.

As mentioned earlier, L-Arg can be oxidized into NO in the H_2O_2-rich and acidic TME. To explore the effect of an acid environment on CPA, the concentration of NO generated in neutral (pH 7.4) and acidic (pH 6.5) solutions was determined *via* a typical Griess assay [60]. As shown in Figure 3k, the reaction rate of L-Arg-H_2O_2 in neutral conditions is very slow, while a burst of NO release is seen at pH 6.5, resulting in NO concentrations ca. 3.4-fold higher than at pH 7.4. The reason for achieving the pH stimuli-responsive NO release may be attributed to the enhanced oxidation properties of H_2O_2 under acidic conditions. It is also worth noting that a negligible concentration of NO is found in the absence of H_2O_2, demonstrating the essential role of H_2O_2 in NO generation through a direct reaction between H_2O_2 and L-Arg. Overall, the presence of L-Arg makes CPA a promising agent for synergistic PTT/GT cancer therapy.
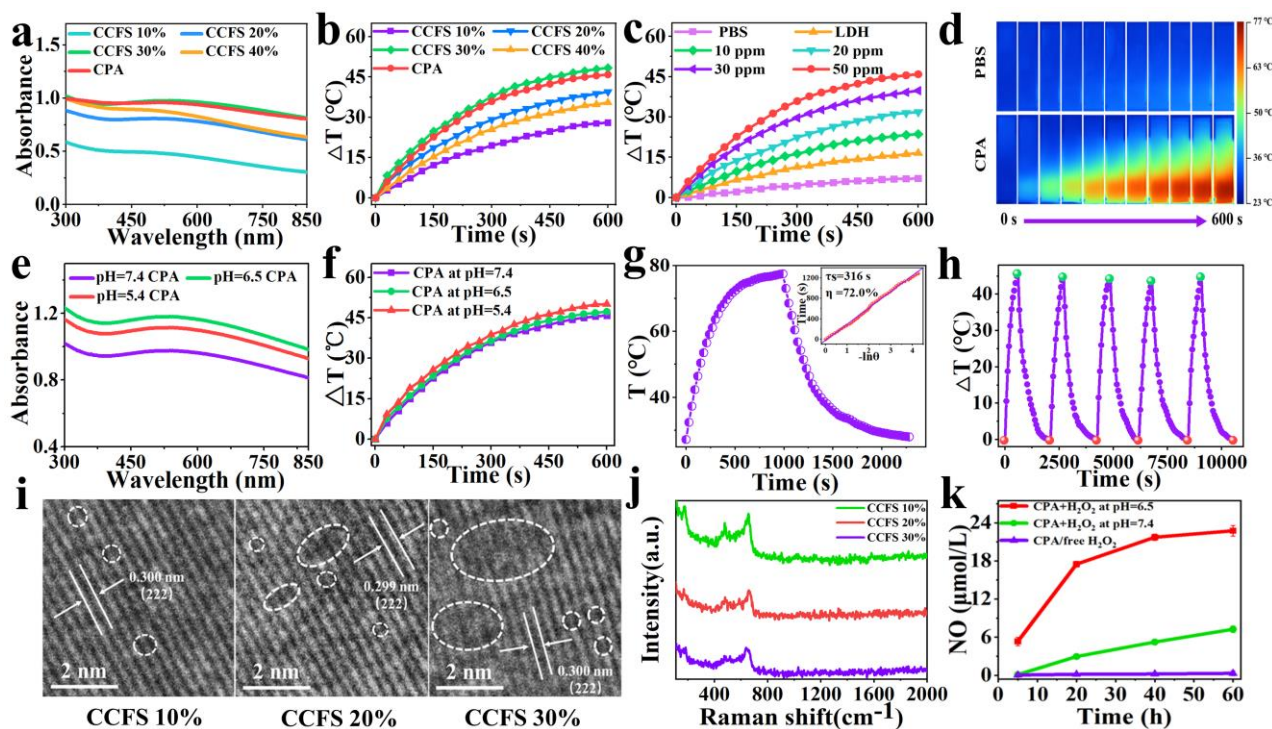
Figure 3. (a) UV–vis absorption spectra of CCFS NSs with various Cu ratios and the CPA nanocomposite (30% Cu). (b) Photothermal effects of CCFS NSs with various Cu ratios and CPA. (c) Photothermal effects of CPA suspensions at various concentrations. (d) Photothermal images of PBS and CPA. (e) UV-vis absorption spectra of CPA at pH 7.4, 6.5 and 5.4. (f) Photothermal effect of CPA at pH 7.4, 6.5 and 5.4. (g) Calculation of photothermal conversion efficiency of CPA at pH 7.4. (h) Photostability tests of CPA over five cycles. (i) HRTEM images of CCFS NSs with various Cu ratios. (j) Raman spectrum of CCFS with various Cu ratios. (k) The NO concentration generated by CPA with or without H_2O_2 under neutral (pH 7.4) or acidic (pH 6.5) conditions. Error bars denote $\pm$ s.d. ($n = 3$). All photothermal experiments were performed with irradiation at 808 nm for 10 min with a power density of 1.0 W cm^{-2}.

3.3 *In vitro* biocompatibility and PTT/GT study.

Prior to studying the anticancer effect of CPA nanocomposite, a biocompatibility evaluation was performed. Three types of cancer cells (U87mg, Hela, HepG2) and COS7 cells were incubated with

18

different concentrations of CPA (0-200 μg mL^{-1}), and then the cell viability was quantified through a standard methyl thiazolyl tetrazolium (MTT) assay. As shown in Figure S16 and S17, no obvious toxicity is observed in any of the cell lines even at a concentration as high as 200 μg mL^{-1}, which indicated that the CPA nanocomposite had excellent biocompatibility. The precursor CoCuFe-LDH NSs also show good biocompatibility, similar to the CPA nanocomposite (Figure 4a).

To study the PTT/GT effects of CPA, HepG2 cells were incubated with LDH, CPA+H$_2$O$_2$, CP and CPA (100 μM) at concentrations ranging from 0-20 μg·mL^{-1} for 24 h. As illustrated in Figure 4b, the cell viabilities of HepG2 cells treated with CoCuFe-LDH, CP and CPA (20 μg mL^{-1}) are 83.3%, 22.3% and 20.4% respectively after 10 min irradiation (1.0 W cm^{-2}). In the presence of 20 μg·mL^{-1} of CPA+H$_2$O$_2$, the cell viabilities are 90.1% (without irradiation) and 8.2% (with irradiation), indicating synergistic PTT/GT effects. To further prove the synergistic effect, the half-maximal inhibitory concentrations (IC$_{50}$) of CPA+H$_2$O$_2$, CP+L and CPA+H$_2$O$_2$+L were calculated to obtain the combination index (CI). The obtained CI value (0.82) is less than 1.0, indicating the excellent synergistic effect of PTT/GT [61].

HepG2 cells treated with saline, LDH, CP, CPA, and CPA+H$_2$O$_2$ respectively (without or with 808 nm irradiation) were stained with calcein acetoxymethyl ester and propidium iodide (calcein-AM/PI; Figure 4c). The results are consistent with the MTT data. When the HepG2 cells were stained with Annexin V-FITC/PI and analyzed by flow cytometry, a 90.5% apoptosis is observed in HepG2 cells treated with CPA+H$_2$O$_2$ and exposed to 808 nm radiation for 10 min. Significant early-stage apoptosis appears in the PI$^+$/Annexin V-FITC$^+$ region, demonstrating that the effective PTT/GT was induced by the CPA nanocomposite (Figure 4d).

NO release in the HepG2 cellular environment was detected by the NO fluorescence probe DAF-FM DA. Compared with the blank group, HepG2 cells incubated with CPA (pH 6.5) and H$_2$O$_2$

alone show no green fluorescence signal while it is obvious in CPA+H_2O_2 (pH 6.5), proving that a large amount of intracellular NO was produced by the CPA nanocomposite reacting with H_2O_2 in the acidic microenvironment (Figure 4e and Figure S18a). The flow cytometer results display markedly increased fluorescence intensity with CPA+H_2O_2, which also confirms the large amount of NO production (Figure 4f and Figure S18b). To explore the potential of the CPA formulation to act as an imaging agent, allowing theranostics as well as treatment, the PA signal was explored for the 30% Cu-doped CPA sample at different concentrations. As is revealed in Figure 4g, as the concentration increased from 0 to 25 μg mL^{-1}, the PA signal is significantly enhanced, presenting a positive linear relationship (Figure 4h). The PA signal of CPA is much stronger than that of the LDH precursor at the same concentration, showing excellent PA performance after selenylation.
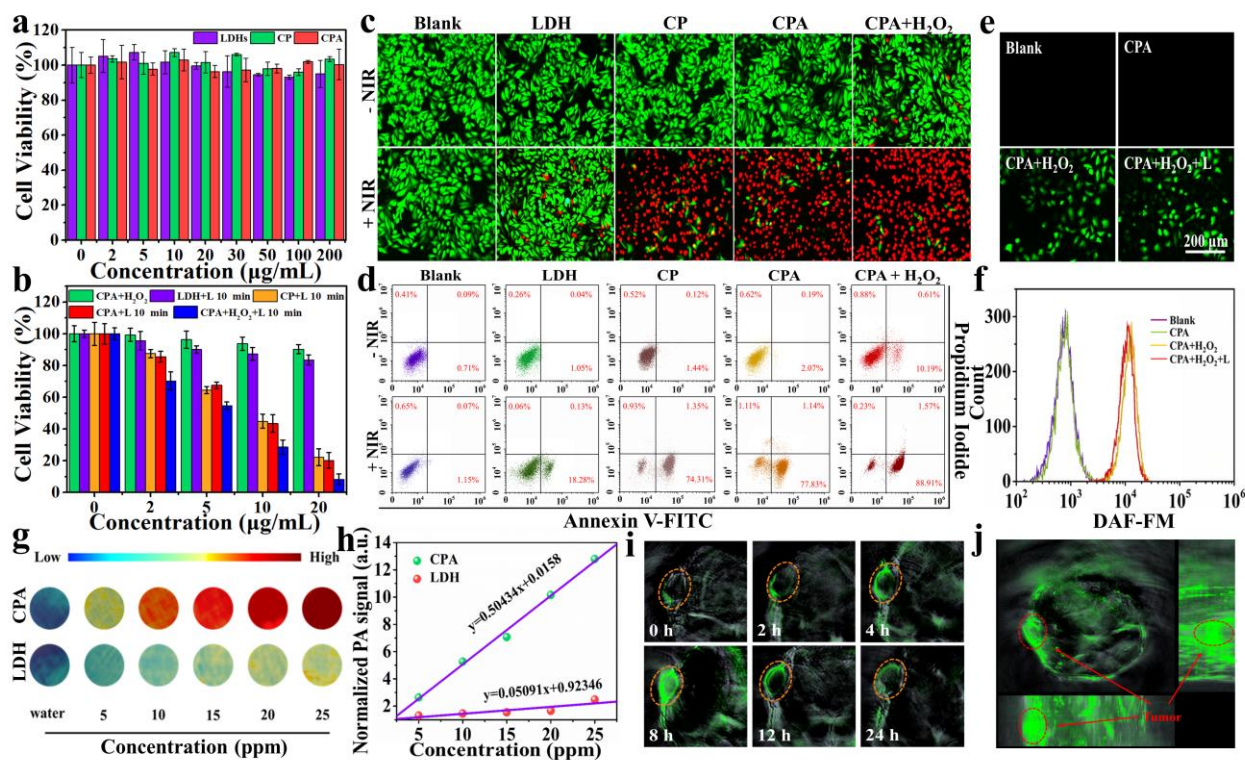
Figure 4. (a) MTT assay results of HepG2 cells after incubation with CoCuFe-LDH and CPA samples at various concentrations. (b) MTT results of HepG2 cells after incubation with CoCuFe-LDH, CPA+H_2O_2, CP and CPA at various concentrations (without or with 808 nm laser

irradiation at a power density of 1.0 W cm^{-2} for 10 min). (c) Corresponding Calcein-AM/PI staining images. The green and red fluorescence represents live and dead cells, respectively. (d) PI/Annexin V-FITC double staining to determine the extent of HepG2 cells apoptosis after different treatments. (e) HepG2 cells stained with the NO fluorescence probe DAF-FM DA after being treated with blank, CPA, CPA+H_2O_2, and CPA+H_2O_2+laser. The green fluorescence intensity represents the NO level. (f) Corresponding fluorescence signal intensity as detected by flow cytometry. (g) PA images and (h) PA intensity of CoCuFe-LDH and CPA aqueous suspensions with various concentrations. (i) *In vivo* PA imaging of the tumor (highlighted by a red circle) at various time points after a mouse was intravenously injected with CPA (dose = 10 mg kg^{-1}). (j) A 3D PA image of tumor at 8 h post-injection, based on image reconstruction. Where shown, error bars denote ± s.d. (*n* = 3).

3.4 *In vivo* anti-tumor therapy

Encouraged by the *in vitro* results, the *in vivo* therapeutic efficacy was evaluated in HepG2 tumor-bearing mice *via* intravenous (*i.v.*) injections (200 μL, 10 mg kg^{-1}). We first assessed the PA performance of CPA in the HepG2 tumor-bearing model (n=3 mice/group). No PA signal is found in the tumor area (Figure 4i, red circle) before injection, but 4 h after *i.v.* injection a clearly distinguishable PA signal begins to appear and peaks after 8 h. The PA signal then decreases rapidly and becomes undetectable 24 h post-injection. Figure 4j gives a 3D PA image 8 h after *i.v.* injection, indicating a distinct accumulation of CPA.

Subsequently, the mice were randomly divided into five groups: (1) PBS+NIR (control group), (2) LDH+NIR, (3) CPA (GT alone), (4) CP (PTT alone), (5) CPA+NIR (PTT/GT). 8 h after the *i.v* administration of 200 μL of sample (10 mg kg^{-1}), the mice were anesthetized and exposed to 808 nm NIR laser (1.0 W cm^{-1}, 7 min). *In vivo* photothermal images to visualize temperature changes

were recorded using an IR thermal camera (Figure 5a). The tumor site temperature of the mice injected with CPA reaches 56.2 °C over the 7 min irradiation, while the groups injected with PBS and LDH show a reduced temperature increase to 38.6 °C and 43.8 °C, respectively.

To quantitatively evaluate the therapeutic effects, the tumor volume was recorded every other day over 16 days of treatment (Figure 5b and c). The PBS group with irradiation exhibits rapid tumor growth, while the LDH+NIR and CPA groups show slight inhibition. In the CP+NIR group, the tumor is suppressed to a certain extent. Impressively, the tumor is completely ablated in the CPA+NIR group during the experimental period. In addition, in the CPA + NIR group, rapid wound healing at the treatment site was also found during the treatment, which may be attributed to that NO can promote the production of various growth factors [62]. And the rapid healing of the wound will further prevent the recurrence of the tumor caused by inflammation [63]. The excellent antitumor effect of CPA plus irradiation can be seen both from digital photos (Figure 5b) and volume curves (Figure 5c). The tumor tissue slices collected from the five treatment groups were stained with hematoxylin and eosin (H&E) (Figure 5d). Very clear necrosis of HepG2 cells is observed in the CPA+NIR group, while the PBS+NIR group maintains a normal cell morphology and the LDH+NIR, CP+NIR and CPA groups show partial necrosis.

The Co concentrations in the major organs and tumor sites were measured by inductively coupled plasma-mass spectrometry (ICP-MS) to investigate the accumulation and metabolism of CPA nanocomposite *in vivo* (Figure 5e). A high level of Co element accumulates in the tumor site at 2~8 h post injection as a result of the enhanced permeability and retention (EPR) effect. Simultaneously, the Co content in lung, liver and spleen reached a high level firstly and then decreased to a very low level at 48 h. The fast decrease of Co content in these organs indicates the easy elimination of CPA [64]. Moreover, after 30 d, the levels of Co element in all the measured

organs and tissues become very low, demonstrating that CPA could be metabolized almost completely from the mice body. Furthermore, no obvious change in body weight is seen throughout the experimental period (Figure 5f), indicating that all these treatments had negligible side effects. No significant difference between the H&E staining images of the major organs (heart, liver, spleen, lung, kidney; Figure 5g) are observed with the CPA and PBS groups. After the mice were treated with CPA nanocomposite, their blood biochemistry indices (WBC, RBC, PLT and HGB) and levels of AST, ALT, BUN and CRE (liver and kidney function indices) show no difference to those of healthy mice, proving negligible side effects of CPA administration (Figure S19) and confirming good biocompatibility *in vivo*.

To probe into the *in vivo* effect of CPA in more detail, an *in situ* tumor model was developed using 4T1 tumor cells labelled with firefly luciferase. Bioluminescence imaging was used to investigate the antitumor performance of CPA through the specific binding of firefly luciferase and fluorescein. This allows rapid, sensitive and noninvasive *in vivo* detection as well as quantitative analysis of tumor growth and metastasis [65-68]. The results are displayed in Figure 5h. The tumors grow rapidly in the PBS control group, but are partly suppressed in the LDH+NIR and CPA groups. In contrast, an obvious decrease in tumor size is observed in the CP+NIR group. More excitingly, in the group treated with CPA and NIR irradiation, the tumors are completely destroyed or became atrophied. All these results confirm that the CPA nanocomposite has excellent synergistic PTT/GT performance and potential clinical applications.
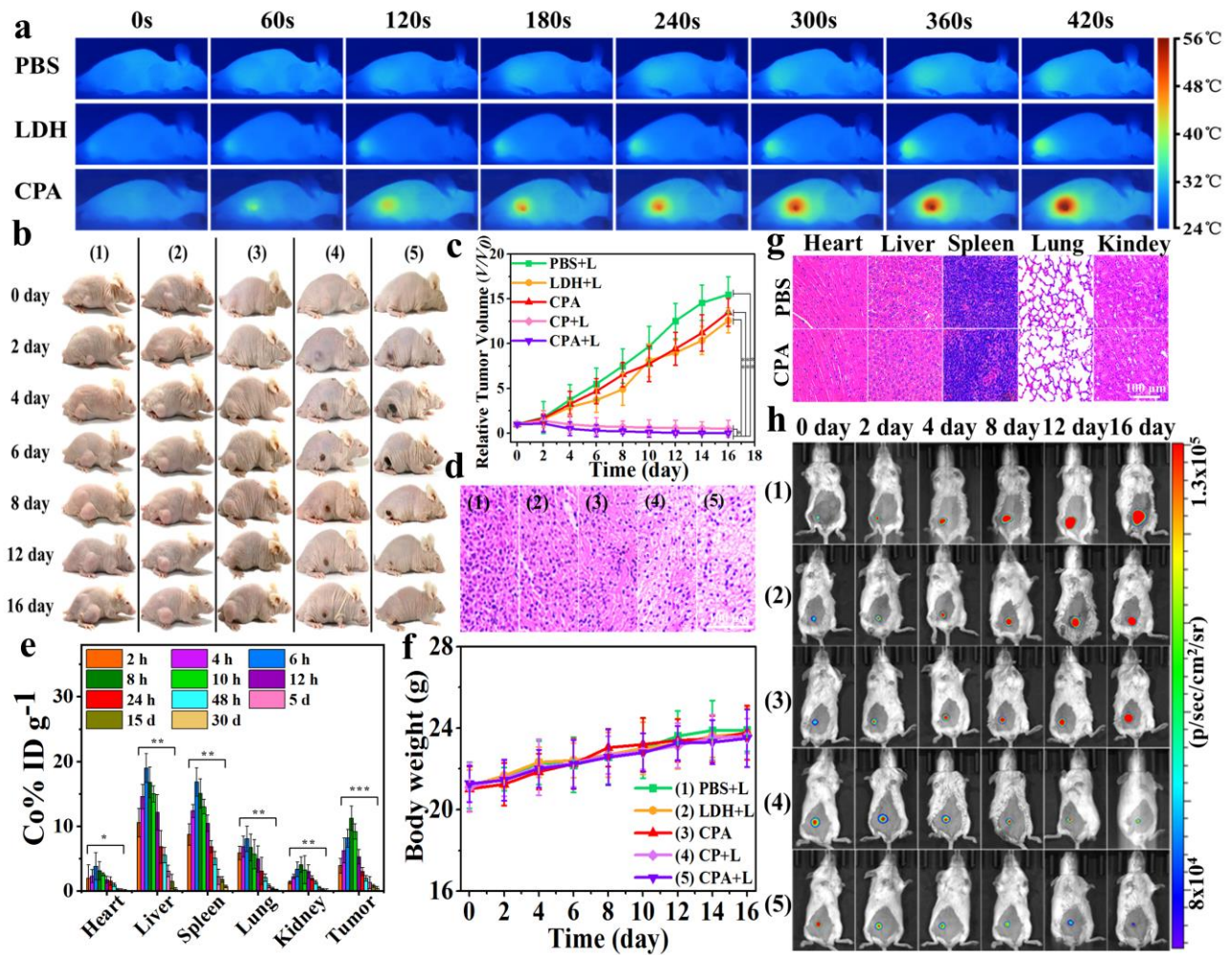
Figure 5. *In vivo* data of mice *i.v.* injected with PBS, CoCuFe-LDH and CPA with 7 min irradiation applied at 8 h post-injection. (a) Photothermal imaging. (b) Digital photographs of mice recorded every other day over 16 days after various treatments. (c) Tumor growth curves (**$p < 0.01$). (d) Tumor tissue slices stained with H&E after 16 days of treatment. (e) Time-dependent distribution of CPA in various organs determined by Co concentration (*$p < 0.05$, **$p < 0.01$, ***$p < 0.001$). (f) Body weight of mice measured every other day. (g) Histological images of major organs treated with PBS and CPA, collected on day 16. (h) Bioluminescence imaging of 4T1-fluc-tumor-bearing mice intravenously injected with PBS, CoCuFe-LDH, CP and CPA without or with NIR laser irradiation for 7 min. Images were taken at day 0, 2, 4, 8, 12, and 16, respectively. Error bars stand for ± s.d. ($n = 6$).

4. Conclusions

An ultrathin chalcogenide nanocomposite was prepared *via* the facile topotactic structural transformation of a precursor CoCuFe-LDH and subsequent surface modification by PVP and L-Arg. The resultant CPA nanocomposite can be used as a novel nanoplatform both for synergistic PTT/GT of tumors and PA imaging. The CPA nanocomposite exhibited a photothermal conversion efficiency of 72.0% and 81.0% at pH 7.4 and 5.4, respectively. These photothermal properties allowed PA imaging to be used to provide noninvasive real-time information on CPA distribution *in vivo*. Moreover, the H_2O_2-rich and acidic tumor microenvironment could trigger the oxidization of L-Arg for effective NO generation and targeted GT. *In vitro* and *in vivo* investigations respectively demonstrated 91.8% apoptosis of HepG2 cells and complete tumor elimination by a synergistic PTT/GT treatment with CPA and 808 nm irradiation. Therefore, this work provides a robust route to construct ultrathin Cu-containing chalcogenides with highly potent photothermal properties coupled with tumor-specific GT, and thus could serve as a useful system for future clinical cancer theranostics.

Supporting Information

Supporting Information is available from the Biomaterials Online Library or from the author.

References

[1] L.Y. Li, Y.M. Zhou, R.Y. Gao, X.C. Liu, H.H. Du, J.L. Zhang, X.C. Ai, J.P. Zhang, L.M. Fu, L.H. Skibsted, Naturally occurring nanotube with surface modification as biocompatible, target-specific nanocarrier for cancer phototherapy, Biomaterials 190–191 (2019) 86–96.

[2] J. Lai, G. Deng, Z. Sun, X. Peng, J. Li, P. Gong, P. Zhang, L. Cai, Scaffolds biomimicking macrophages for a glioblastoma NIR-Ib imaging guided photothermal therapeutic strategy by crossing Blood-Brain Barrier, Biomaterials 211 (2019) 48–56.

[3] Z. Tang, P. Zhao, D. Ni, Y. Liu, M. Zhang, H. Wang, H. Zhang, H. Gao, Z. Yao, W. Bu, Pyroelectric nanoplatform for NIR-II-triggered photothermal therapy with simultaneous pyroelectric dynamic therapy, Mater. Horiz. 5 (2018) 946–952.

[4] G. Gao, Y.W. Jiang, H.R. Jia, W. Sun, Y. Guo, X.W. Yu, X. Liu, F.G. Wu, From perinuclear to intranuclear localization: A cell-penetrating peptide modification strategy to modulate cancer cell migration under mild laser irradiation and improve photothermal therapeutic performance, Biomaterials 223 (2019) 119443.

[5] Z. Meng, F. Wei, R. Wang, M. Xia, Z. Chen, H. Wang, M. Zhu, NIR-Laser-Switched In Vivo Smart Nanocapsules for Synergic Photothermal and Chemotherapy of Tumors, Adv. Mater. 28 (2016) 245–253.

[6] M. Qiua, A. Singhb, D. Wangc, J. Qua, M. Swihart, H. Zhang, P.N. Prasad, Biocompatible and biodegradable inorganic nanostructures for nanomedicine: Silicon and black phosphorus, Nano Today 25 (2019) 135–155.

[7] X. Ji, N. Kong, J. Wang, W. Li, Y. Xiao, S.T. Gan, Y. Zhang, Y. Li, X. Song, Q. Xiong, S. Shi, Z. Li, W. Tao, H. Zhang, L. Mei, J. Shi, A Novel Top-Down Synthesis of Ultrathin 2D Boron

Nanosheets for Multimodal Imaging-Guided Cancer Therapy, Adv. Mater. 30 (2018) 1803031.

[8] W. Tao, X. Ji, X. Zhu, L. Li, J. Wang, Y. Zhang, P.E. Saw, W. Li, N. Kong, M.A. Islam, T. Gan, X. Zeng, H. Zhang, M. Mahmoudi, G.J. Tearney, O.C. Farokhzad, Two-Dimensional Antimonene-Based Photonic Nanomedicine for Cancer Theranostics, Adv. Mater. 30 (2018) 1802061.

[9] X. Zheng, D. Xing, F. Zhou, B. Wu, W.R. Chen, Indocyanine Green-Containing Nanostructure as near Infrared Dual-Functional Targeting Probes for Optical Imaging and Photothermal Therapy. Mol. Pharmaceutics 8 (2011) 447–456.

[10] S. Chen, C. Xing, D. Huang, C. Zhou, B. Ding, Z. Guo, Z. Peng, D. Wang, X. Zhu, S. Liu, Z. Cai, J. Wu, J. Zhao, Z. Wu, Y. Zhang, C. Wei, Q. Yan, H. Wang, D. Fan, L. Liu, H. Zhang, Y. Cao, Eradication of tumor growth by delivering novel photothermal selenium-coated tellurium nanoheterojunctions, Science Advances 6 (2020) 6825.

[11] C. Xing, S. Chen, X. Liang, Q. Liu, M. Qu, Q. Zou, J. Li, H. Tan, L. Liu, D. Fan, H. Zhang, Two-Dimensional MXene (Ti$_3$C$_2$)-Integrated Cellulose Hydrogels: Toward Smart Three-Dimensional Network Nanoplatforms Exhibiting Light-Induced Swelling and Bimodal Photothermal/Chemotherapy Anticancer Activity, ACS Appl. Mater. Interfaces 10 (2018) 27631–27643.

[12] S. Liu, X. Pan, H. Liu, Two-Dimensional Nanomaterials for Photothermal Therapy, Angew. Chem. Int. Ed. 59 (2020) 2–13.

[13] T. Hu, X. Mei, Y. Wang, X. Weng, R. Liang, M. Wei, Two-dimensional nanomaterials: fascinating materials in biomedical field, Science Bulletin 64 (2019) 1707–1727.

[14] T.H. Yang, K.C. Chiu, Y.W. Harn, H.Y. Chen, R.F. Cai, J.J. Shyue, S.C. Lo, J.M. Wu, Y.H. Lee, Electron Field Emission of Geometrically Modulated Monolayer Semiconductors, Adv. Funct.

Mater. 28 (2018) 1706113.

[15] C. Martella, C. Mennucci, A. Lamperti, E. Cappelluti, F.B. de Mongeot, A. Molle, Designer Shape Anisotropy on Transition-Metal-Dichalcogenide Nanosheets, Adv. Mater. 30 (2018) 1705615.

[16] V. Urbanova, M. Pumera, Biomedical and bioimaging applications of 2D pnictogens and transition metal dichalcogenides, Nanoscale 11 (2019) 15770–15782.

[17] Y. Chen, Z. Fan, Z. Zhang, W. Niu, C. Li, N. Yang, B. Chen, H. Zhang, Two-Dimensional Metal Nanomaterials: Synthesis, Properties, and Applications, Chem. Rev. 118 (2018) 6409–6455.

[18] X. He, C. Peng, S. Qiang, L.H. Xiong, Z. Zhao, Z. Wang, R.T.K. Kwok, J.W.Y. Lam, N. Ma, B.Z. Tang, Less is more: Silver-AIE core@shell nanoparticles for multimodality cancer imaging and synergistic therapy, Biomaterials 238 (2020) 119834.

[19] Q. Wang, J. Xu, R. Geng, J. Cai, J. Li, C. Xie, W. Tang, Q. Shen, W. Huang, Q. Fan, High performance one-for-all phototheranostics: NIR-II fluorescence imaging guided mitochondria-targeting phototherapy with a single-dose injection and 808 nm laser irradiation, Biomaterials 231 (2020) 119671.

[20] D. Zhang, T. Wu, X. Qin, Q. Qiao, L. Shang, Q. Song, C. Yang, Z. Zhang, Intracellularly Generated Immunological Gold Nanoparticles for Combinatorial Photothermal Therapy and Immunotherapy against Tumor, Nano Lett. 19 (2019) 6635–6646.

[21] Z. He, L. Zhao, Q. Zhang, Mei. Chang, C. Li, H. Zhang, Y. Lu, Y. Chen, An Acceptor-Donor-Acceptor Structured Small Molecule for Effective NIR Triggered Dual Phototherapy of Cancer, Adv. Funct. Mater. 30 (2020) 1910301.

[22] Y. Xuan, X.Q. Yang, Z.Y. Song, R.Y. Zhang, D.H. Zhao, X.L. Hou, X.L. Song, B. Liu, Y.D. Zhao, W. Chen, High-Security Multifunctional Nano-Bismuth-Sphere-Cluster Prepared from Oral

Gastric Drug for CT/PA Dual-Mode Imaging and Chemo-Photothermal Combined Therapy In Vivo, Adv. Funct. Mater. 29 (2019) 1900017.

[23] M.R. Younis, C. Wang, R. An, S. Wang, M.A. Younis, Z.Q. Li, Y. Wang, A. Ihsan, D. Ye, X.H. Xia, Low Power Single Laser Activated Synergistic Cancer Phototherapy Using Photosensitizer Functionalized Dual Plasmonic Photothermal Nanoagents, ACS Nano 13 (2019) 2544–2557.

[24] S. Liang, X. Deng, Y. Chang, C. Sun, S. Shao, Z. Xie, X. Xiao, P. Ma, H. Zhang, Z. Cheng, J. Lin, Intelligent Hollow Pt-CuS Janus Architecture for Synergistic Catalysis-Enhanced Sonodynamic and Photothermal Cancer Therapy, Nano Lett. 19 (2019) 4134–4145.

[25] L. Yu, P. Hu, Y. Chen, Gas-Generating Nanoplatforms: Material Chemistry, Multifunctionality, and Gas Therapy, Adv. Mater. 30 (2018) 1801964.

[26] P. Zhao, Z. Jin, Q. Chen, T. Yang, D. Chen, J. Meng, X. Lu, Z. Gu, Q. He, Local generation of hydrogen for enhanced photothermal therapy, Nat. Commun. 9 (2018) 4241.

[27] C. Zhang, D.W. Zheng, C.X. Li, M.Z. Zou, W.Y. Yu, M.D. Liu, S.Y. Peng, Z.L. Zhong, X.Z. Zhang, Hydrogen gas improves photothermal therapy of tumor and restrains the relapse of distant dormant tumor, Biomaterials 223 (2019) 119472.

[28] Y. Liu, F. Yang, C. Yuan, M. Li, T. Wang, B. Chen, J. Jin, P. Zhao, J. Tong, S. Luo, N. Gu, Magnetic Nanoliposomes as in Situ Microbubble Bombers for Multimodality Image-Guided Cancer Theranostics, ACS Nano 11 (2017) 1509–1519.

[29] M. Xu, Q. Lu, Y. Song, L. Yang, J. Li, N. Li, Enhanced Bax upregulating in mitochondria for deep tumor therapy based on SO_2 prodrug loaded Au-Ag hollow nanotriangle, Biomaterials 250 (2020) 120076.

[30] L. Chen, S.F. Zhou, L. Su, J. Song, Gas-Mediated Cancer Bioimaging and Therapy, ACS Nano

13 (2019) 10887–10917.

[31] W. Fan, B.C. Yung, X. Chen, Stimuli-Responsive NO Release for On-Demand Gas-Sensitized Synergistic Cancer Therapy, Angew. Chem. Int. Ed. 57 (2018) 8383–8394.

[32] K. Zhang, H. Xu, X. Jia, Y. Chen, M. Ma, L. Sun, H. Chen, Ultrasound-Triggered Nitric Oxide Release Platform Based on Energy Transformation for Targeted Inhibition of Pancreatic Tumor, ACS Nano 10 (2016) 10816–10828.

[33] Y. Ding, C. Du, J. Qian, C.M. Dong, NIR-Responsive Polypeptide Nanocomposite Generates NO Gas, Mild Photothermia, and Chemotherapy to Reverse Multidrug-Resistant Cancer, Nano Lett. 19 (2019) 4362–4370.

[34] W. Fan, N. Lu, P. Huang, Y. Liu, Z. Yang, S. Wang, G. Yu, Y. Liu, J. Hu, Q. He, J. Qu, T. Wang, X. Chen, Glucose-Responsive Sequential Generation of Hydrogen Peroxide and Nitric Oxide for Synergistic Cancer Starving-Like/Gas Therapy, Angew. Chem. Int. Ed. 56 (2017) 1229–1233.

[35] S. Zhang, C. Sun, J. Zeng, Q. Sun, G. Wang, Y. Wang, Y. Wu, S. Dou, M. Gao, Z. Li, Ambient Aqueous Synthesis of Ultrasmall PEGylated $Cu_{2-x}Se$ Nanoparticles as a Multifunctional Theranostic Agent for Multimodal Imaging Guided Photothermal Therapy of Cancer, Adv. Mater. 28 (2016) 8927–8936.

[36] X. Jiang, S. Zhang, F. Ren, L. Chen, J. Zeng, M. Zhu, Z. Cheng, M. Gao, Z. Li, Ultrasmall Magnetic $CuFeSe_2$ Ternary Nanocrystals for Multimodal Imaging Guided Photothermal Therapy of Cancer, ACS Nano 11 (2017) 5633–5645.

[37] B. Li, J. Tang, W. Chen, G. Hao, N. Kurniawan, Z. Gu, Z.P. Xu, Novel theranostic nanoplatform for complete mice tumor elimination via MR imaging-guided acid-enhanced photothermo-/chemo-therapy, Biomaterials 177 (2018) 40–51.

[38] B. Li, F. Yuan, G. He, X. Han, X. Wang, J. Qin, Z.X. Guo, X. Lu, Q. Wang, I.P. Parkin, C. Wu, Ultrasmall $CuCo_2S_4$ Nanocrystals: All-in-One Theragnosis Nanoplatform with Magnetic Resonance/Near-Infrared Imaging for Efficiently Photothermal Therapy of Tumors, Adv. Funct. Mater. 27 (2017) 1606218.

[39] J. Cui, R. Jiang, C. Guo, X. Bai, S. Xu, L. Wang, Fluorine Grafted Cu_7S_4-Au Heterodimers for Multimodal Imaging Guided Photothermal Therapy with High Penetration Depth, J. Am. Chem. Soc. 140 (2018) 5890–5894.

[40] T. Xing, S. Mateti, L.H. Li, F.X. Ma, A.J. Du, Y. Gogotsi, Y. Chen, Gas Protection of Two-Dimensional Nanomaterials from High-Energy Impacts, Sci. Rep. 6 (2016) 35532.

[41] X.B. Fan, P.T. Xu, Y.C. Li, D.K. Zhou, Y.F. Sun, M.A.T. Nguyen, M. Terrones, T.E. Mallouk, Controlled Exfoliation of MoS_2 Crystals into Trilayer Nanosheets, J. Am. Chem. Soc. 138 (2016) 5143–5149.

[42] G. Guan, S. Zhang, S. Liu, Y. Cai, M. Low, C.P. Teng, I.Y. Phang, Y. Cheng, K.L. Duei, B.M. Srinivasan, Y. Zheng, Y.-W. Zhang, M.-Y. Han, Protein Induces Layer-by-Layer Exfoliation of Transition Metal Dichalcogenides, J. Am. Chem. Soc. 137 (2015) 6152–6155.

[43] G. Zhang, J. Wang, Z. Wu, R. Shi, W. Ouyang, A. Amini, B.N. Chandrashekar, N. Wang, C. Cheng, Shape-Dependent Defect Structures of Monolayer MoS_2 Crystals Grown by Chemical Vapor Deposition, ACS Appl. Mater. Interfaces 9 (2017) 763–770.

[44] C. Tan, H. Zhang, Wet-chemical synthesis and applications of non-layer structured two-dimensional nanomaterials, Nat. Commun.6 (2015) 7873.

[45] Y. Zhao, G. Chen, T. Bian, C. Zhou, G.I.N. Waterhouse, L.Z. Wu, C.H. Tung, L.J. Smith, D. O'Hare, T. Zhang, Defect-Rich Ultrathin ZnAl-Layered Double Hydroxide Nanosheets for Efficient Photoreduction of CO_2 to CO with Water, Adv. Mater. 27 (2015) 7824–7831.

[46] Y. Wang, Y. Zhang, Z. Liu, C. Xie, S. Feng, D. Liu, M. Shao, S. Wang, Layered Double Hydroxide Nanosheets with Multiple Vacancies Obtained by Dry Exfoliation as Highly Efficient Oxygen Evolution Electrocatalysts, Angew. Chem. Int. Ed. 56 (2017) 5867–5871.

[47] G. Yilmaz, K.M. Yam, C. Zhang, H.J. Fan, G.W. Ho, In Situ Transformation of MOFs into Layered Double Hydroxide Embedded Metal Sulfides for Improved Electrocatalytic and Supercapacitive Performance, Adv. Mater. 29 (2017) 1606814.

[48] W. Liu, S. Xu, S. Guan, R. Liang, M. Wei, D.G. Evans, X. Duan, Confined Synthesis of Carbon Nitride in a Layered Host Matrix with Unprecedented Solid-State Quantum Yield and Stability, Adv. Mater. 30 (2018) 1704376.

[49] X. Gao, X. Liu, D. Wu, B. Qian, Z. Kou, Z. Pan, Y. Pang, L. Miao, J. Wang, Significant Role of Al in Ternary Layered Double Hydroxides for Enhancing Electrochemical Performance of Flexible Asymmetric Supercapacitor, Adv. Funct. Mater. 29 (2019) 1903879.

[50] Z. Li, H. Duan, M. Shao, J. Li, D. O'Hare, M. Wei, Z.L. Wang, Ordered-Vacancy-Induced Cation Intercalation into Layered Double Hydroxides: A General Approach for High-Performance Supercapacitors, Chem 4 (2018) 2168–2179.

[51] R. Gao, D. Yan, Fast formation of single-unit-cell-thick and defect-rich layered double hydroxide nanosheets with highly enhanced oxygen evolution reaction for water splitting, Nano Res. 11 (2018) 1883–1894.

[52] R. Gao, X. Mei, D. Yan, R. Liang, M. Wei, Nano-photosensitizer based on layered double hydroxide and isophthalic acid for singlet oxygenation and photodynamic therapy, Nat. Commun. 9 (2018) 2798.

[53] B. Li, G. Hao, B. Sun, Z. Gu, Z.P. Xu, Engineering a Therapy-Induced "Immunogenic Cancer Cell Death"Amplifier to Boost Systemic Tumor Elimination, Adv. Funct. Mater. 30 (2020)

1909745.

[54] X. Mei, S. Xu, T. Hu, L. Peng, R. Gao, R. Liang, M. Wei, D.G. Evans, X. Duan, Layered double hydroxide monolayers for controlled loading and targeted delivery of anticancer drugs, Nano Res. 11 (2018) 195–205.

[55] L. Peng, X. Mei, J. He, J. Xu, W. Zhang, R. Liang, M. Wei, D.G. Evans, X. Duan, Monolayer Nanosheets with an Extremely High Drug Loading toward Controlled Delivery and Cancer Theranostics, Adv. Mater. 30 (2018) 1707389.

[56] W. Tao, N. Kong, X. Ji, Y. Zhang, A. Sharma, J. Ouyang, B. Qi, J. Wang, N. Xie, C. Kang, H. Zhang, O.C. Farokhzad, J.S. Kim, Emerging two-dimensional monoelemental materials (Xenes) for biomedical applications, Chem. Soc. Rev. 48 (2019) 2891–2912.

[57] M. Qiu, W.X. Ren, T. Jeong, M. Won, G.Y. Park, D.K. Sang, L.P. Liu, H. Zhang, J.S. Kim, Omnipotent phosphorene: a next-generation, two-dimensional nanoplatform for multidisciplinary biomedical applications, Chem. Soc. Rev. 47 (2018) 5588–5601.

[58] I. Lopes, N.E. Hassan, H. Guerba, G. Wallez, A. Davidson, Size-Induced Structural Modifications Affecting Co_3O_4 Nanoparticles Patterned in SBA-15 Silicas, Chem. Mater. 18 (2006) 5826–5828.

[59] B. Mallesham, P. Sudarsanam, G. Raju, B.M. Reddy, Design of highly efficient Mo and W-promoted SnO_2 solid acids for heterogeneous catalysis: acetalization of bio-glycerol, Green Chem. 15 (2013) 478–489.

[60] K. Chegaev, A. Fraix, E. Gazzano, G.E.F. Abd-Ellatef, M. Blangetti, B. Rolando, S. Conoci, C. Riganti, R. Fruttero, A. Gasco, S. Sortino, Light-Regulated NO Release as a Novel Strategy To Overcome Doxorubicin Multidrug Resistance, ACS Med. Chem. Lett. 8 (2017) 361–365.

[61] S.H. Liu, Y.B. Guo, R.Q. Huang, J.F. Li, S.X. Huang, Y.Y. Kuang, L. Han and C. Jiang, Gene

and doxorubicin co-delivery system for targeting therapy of glioma, Biomaterials 33 (2012) 4907.

[62] T. Suzuki, S. Wada, N. Tomizawa, R. Kamata, S. Saito, I. Sato, E. Sugawara, E. Tachikawa, H. Kobayashi, A Possible Role Nitric Oxide Formation in the Vasodilatation of Rabbit Ear Artery Induced by a Topically Applied Capsaicin Analogue, J Vet Med Sci 60 (1998) 69l–697.

[63] A. Kuraishy, M. Karin, S. I. Grivennikov, Tumor Promotion via Injury- and Death-Induced Inflammation, Immunity 35 (2011) 467–477.

[64] S. Zada, W. Dai, Z. Kai, H. Lu, X. Meng, Y. Zhang, Y. Cheng, F. Yan, P. Fu, X. Zhang, H. Dong, Algae Extraction Controllable Delamination of Vanadium Carbide Nanosheets with Enhanced Near-Infrared Photothermal Performance, Angew. Chem. Int. Ed. 59 (2020) 6601–6606.

[65] M. Zheng, Y. Liu, Y. Wang, D. Zhang, Y. Zou, W. Ruan, J. Yin, W. Tao, J.B. Park, B. Shi, ROS-Responsive Polymeric siRNA Nanomedicine Stabilized by Triple Interactions for the Robust Glioblastoma Combinational RNAi Therapy, Adv. Mater. 31 (2019) 1903277.

[66] S.W. Chung, J.U. Choi, Y.S. Cho, H.R. Kim, T.H. Won, P. Dimitrion, O.C. Jeon, S.W. Kim, I.S. Kim, S.Y. Kim, Y. Byun, Self-Triggered Apoptosis Enzyme Prodrug Therapy (STAEPT): Enhancing Targeted Therapies via Recurrent Bystander Killing Effect by Exploiting Caspase-Cleavable Linker, Adv. Sci. 5 (2018) 1800368.

[67] C. Liu, S. Zhang, J. Li, J. Wei, K. Mullen, M. Yin, A Water-Soluble, NIR-Absorbing Quaterrylenediimide Chromophore for Photoacoustic Imaging and Efficient Photothermal Cancer Therapy, Angew. Chem. Int. Ed. 58 (2019) 1638–1642.

[68] W. Song, K. Tiruthani, Y. Wang, L. Shen, M. Hu, O. Dorosheva, K. Qiu, K.A. Kinghorn, R. Liu, L. Huang, Trapping of Lipopolysaccharide to Promote Immunotherapy against Colorectal Cancer and Attenuate Liver Metastasis, Adv. Mater. 30 (2018) 1805007.

The Table of Contents Entry

Cu-loaded CoCuFe-selenide (CCFS) are synthesized *via* an *in situ* selenylation treatment of ultrathin CoCuFe-LDH precursors, followed by surface modification with polyvinyl pyrrolidone (PVP) and L-arginine (L-Arg). The as-prepared CCFS-PVP-L-Arg (CPA) nanocomposite exhibits excellent performance in photoacoustic (PA) imaging and synergistic photothermal and gas therapy (PTT/GT), which holds great promise for future clinical cancer theranostics.

Keywords: Ultrathin Cu chalcogenide, Layered double hydroxide, Topotactic transformation, Synergistic therapy

Jingjing Wu, Gareth R. Williams, Yu Zhu, Tingting Hu, Hui Wang, Wei Zhao, Ruizheng Liang,* Xisheng Weng,* Min Wei*

Ultrathin Chalcogenide Nanosheets for Photoacoustic Imaging-Guided Synergistic Photothermal/Gas Therapy